

Light Management through Organic Bulk Heterojunction and Carrier Interfacial Engineering for Perovskite Solar Cells with 23.5% Efficiency

Zhichong Shi, Donglei Zhou,* Xinmeng Zhuang, Shuainan Liu, Rui Sun, Wen Xu, Le Liu, and Hongwei Song*

Light management through organic bulk heterojunction (BHJ) has been widely reported to push up the performance of lead-based perovskite solar cells (PSCs) by extending the spectral response. However, the development of integrated perovskite/organic bulk heterojunction solar cells (IPSCs) encounters a bottleneck problem that the poor carrier extraction capability of perovskite and BHJ leads to the severe loss of open-voltage (V_{oc}) and fill factor (FF). Herein, the strategy of introducing black phosphorous quantum dots (BPQDs) and cuprous oxide (CuO_x) into IPSCs is adopted, which not only successfully extends the single-component PSCs light response to 930 nm, but also significantly reduces the V_{oc} and FF loss of IPSCs. BPQDs with bipolar charge transport and high mobility characteristics improves the electron/hole transport behaviors of perovskite and BHJ films. CuO_x with matching energy levels is introduced between BHJ and Spiro-OMeTAD as a buffer layer, which provides good driving force for the transportation of holes. The champion device achieves a power conversion efficiency of 23.52%. The IPSCs devices also display an excellent long-term and humidity stability. This work demonstrates an approach to solve the carrier extraction key issues that limits the performance of IPSCs, which achieves an instructive result in the development of PSCs light management.

1. Introduction

Perovskite solar cells (PSCs) are becoming a revolutionary photovoltaic technology with the potential to disrupt the mature silicon solar cell market, which have achieved the certified power conversion efficiency (PCE) of 25.7%.^[1,2] The impressive progress of the PSC technology is mainly attributed to the extensive optimization of device structure, perovskite composition, device stability, and interfacial charge transport layers.^[3] The development of PCE in the single-cell PSC is limited by the Shockley–Queisser theoretical limit (for example at 30% PCE for the 1.6 eV bandgap methylammonium lead iodide layer),

which greatly limits the PCE improvement space of the single-cell PSCs.^[4] It is an efficient approach to alloy Pb and Sn in metal halide perovskites to obtain narrow bandgaps (E_g) down to 1.17 eV for Sn content of 50–60%.^[5] However, a key limitation in these perovskites is the instability of Sn^{2+} . Sn^{2+} is prone to oxidation, forming Sn^{4+} , especially in precursor solutions and SnI_2 solids, leading to high trap densities and short diffusion lengths in tin-containing perovskites.^[6]

Organic bulk heterojunction (BHJ) has been widely investigated to integrate in the PSCs device to form a multijunction integrated perovskite/organic bulk heterojunction solar cells (IPSC), which absorbs a wider solar spectrum wavelength range to compensate for the narrow light response range (300–800 nm) of the traditional lead-based PSCs.^[7–10] The multijunction IPSC can extend the absorption wavelength to the infrared region and achieve a PCE of more than 40% theoretically.

Although IPSC has successfully expanded the light response range, there is a key element that limits its further development and discourages many researchers.^[11,12] The inherent charge transport properties of BHJ and perovskite films prevent the efficient transport of photogenerated charge carriers between the perovskite layer and the BHJ layer, which leads to the accumulation of charges at the perovskite/BHJ interface. The accumulated charge carriers will cause harmful recombination of charge carriers, which will reduce the surface photovoltage of the photoactive layer and reduce the efficiency of the device through the loss of filling factor. The incomplete collection of photogenerated carriers is the key factor that hinders the IPSC to move toward practicality.^[11,13]

Recently, a series of strategies, such as interface engineering and component engineering, have been explored to solve the problem of carrier recombination in the IPSC interface and the multisource active layer.^[14,15] Chen et al. proposed a recasting strategy that they used the difference in solubility of the two components in the BHJ film to selectively remove the nonfullerene acceptor (NFA) material on the upper part of the BHJ film, which can reduce the contact area between the acceptor material and the HTL and achieve the purpose of inhibiting hole recombination.^[9] Wang et al. optimized the mass ratio of

Z. Shi, D. Zhou, X. Zhuang, S. Liu, R. Sun, W. Xu, L. Liu, H. Song
 State Key Laboratory of Integrated Optoelectronics
 College of Electronic Science and Engineering
 Jilin University
 Changchun 130012, China
 E-mail: zhoudl@jlu.edu.cn; songhw@jlu.edu.cn

The ORCID identification number(s) for the author(s) of this article can be found under <https://doi.org/10.1002/adfm.202203873>.

DOI: 10.1002/adfm.202203873

organic donor/NFA materials and constructed a double continuous interpenetrating network to optimize the vertical distribution of organic donor and NFA in the BHJ film space.^[12] Although these measures suppressed the recombination of the photogenerated carriers inside the BHJ/HTL and BHJ films to a certain extent, a considerable loss of FF and V_{oc} was still observed. Active layer selective doping and selective contact HTL have been widely used in silicon or other thin-film photovoltaic technologies to enhance charge extraction and reduce recombination at the interfaces.^[14,16–21] BPQDs is a newly emerging material, which has attracted widespread attentions due to the anisotropy and unique semiconductor properties (charge bipolar transport). BPQD has a size-adjustable forbidden band width, high absorption coefficient, high carrier mobility ($\sim 1000 \text{ cm}^2 \text{ V}^{-1} \text{ s}^{-1}$) and unique self-repair characteristics.^[22–26] It has been incorporated into PSC devices to promote light collection in the active layer and serve as a hole/electron transport material. For example, Yi and Li et al. exploited the synergy of the PFN-Br/BPQDs heterointerface, which provided additional built-in electric field and transport pathways. Guo and Xu et al. utilized BPQDs to modify the SnO_2 ETL, which effectively enhanced the electron extraction efficiency of PSCs. Yi and Min et al. utilized BPQDs to optimize the morphology of the inorganic perovskite CsPbI_2Br and provide a more efficient route for electron extraction inside the device. Song and Zhou et al. tuned the carrier transport inside the device by introducing BPQDs in HTL, which enabled PSCs to obtain a V_{oc} of 1.235 V.^[27–33] These characteristics allow it to act as a high-speed electron/hole transport channel by involving in the perovskite films and BHJ films, enhancing charge extraction and reducing the recombination of electrons/holes in the perovskite/BHJ.^[34]

In typical IPSC, BHJ was introduced by spin-coating a BHJ chlorobenzene solution in one step, which greatly limited the choice of HTL for IPSC. The HTL usually adopt inorganic materials like MoO_x (a high-work function n-type oxide) prepared by magnetron sputtering and evaporation method, which greatly affects its extraction of photogenerated holes between BHJ/perovskite interface.^[35–37] The accumulation of photogenerated carriers at the perovskite/BHJ interface will cause severe interface reorganization, which will deteriorate the overall FF and V_{oc} .^[11] Due to the poor hole mobility of high-work function n-type oxides, it is important to construct a p-type HTL that can efficiently extract photogenerated holes.^[38] It is suggested that the double-layer HTL with matching energy levels seems to be an effective measure to solve this problem. The p-type CuO_x layer has excellent hole mobility ($4.5 \pm 2 \text{ cm}^2 \text{ V}^{-1} \text{ s}^{-1}$) and hole extraction ionization potential, which is a suitable candidate to serve as a buffer layer for constructing double-layer HTL.^[39]

In this work, organic conjugated donor PM6 and NFA BTP-4Cl-12 composed of BHJ active layer were directly deposited on the perovskite active layer to construct IPSC device with near-infrared absorption capability (800–930 nm). Here, for the first time, BPQDs were simultaneously incorporated into perovskite films and BHJ films in IPSC, which enhanced their photo-generated electron/photogenerated hole transport capabilities. The carrier recombination at the perovskite/BHJ interface was inhibited and the loss of FF and V_{oc} of IPSC was significantly eliminated. P-type CuO_x with excellent hole mobility and matched hole extraction ionization potential was introduced

into IPSC as a buffer layer, which reduced the carrier recombination between BHJ/HTL and improved the overall performance of IPSC. As a result, IPSC achieved 51% maximum light response value in the infrared region of 800–930 nm and a higher short-circuit current density without sacrificing V_{oc} and FF. The champion device has obtained a PCE of 23.52%. This research has broken the development bottleneck in the IPSC field, that is, using NIR can make significant improvements to PCE in practice.

2. Results and Discussions

We have manufactured IPSC devices based on FTO/ SnO_2 /Perovskite-BPQDs/BHJ-BPQDs/ CuO_x /Spiro-OMeTAD/Ag structure. The complete device structure concept diagram of IPSC is shown in Figure 1a. The perovskite precursor solution composed of $(\text{FA}_{0.85}\text{MA}_{0.15})\text{Pb}(\text{I}_{0.85}\text{Br}_{0.15})_3$ was deposited on top of SnO_2 as the active layer by a one-step spin coating method. The BHJ film composed of PM6:BTP-4Cl-12 was deposited directly on top of the perovskite layer as a multisource active layer. Then, CuO_x was deposited through dc reactive magnetron sputtering method acting as a p-type contact buffer layer. Spiro-OMeTAD was deposited on CuO_x as the second HTL. As shown in Figure 1b, the NFA BTP-4Cl-12 in the BHJ film and the perovskite film exhibits complementary light absorption. The absorption edge of the NFA BTP-4Cl-12 film locates at 960 nm. Meanwhile, the decrease in transmittance proves that the organic donor PM6: BTP-4Cl-12 can also enhance the light absorption of IPSC in the range of 300–1000 nm (Figure S1, Supporting Information). The chemical structures of black phosphorus, PM6 and BTP-4Cl-12 are shown in Figure 1c. The conceptual diagram of the structure of BPQDs is shown in Figure S2 (Supporting Information).

As shown in Figure 2a,b, the transmission electron microscopy (TEM) measurement was performed to characterize the morphology of BPQDs. Through a simple ultrasonic liquid peeling technique, we prepared BPQDs with uniform size distribution.^[40] The high-resolution TEM (HR-TEM) image in Figure 2c exhibits lattice fringes of 0.256 nm, which is consistent with the (111) plane of the BP crystal. Figure 2d shows the top-view scanning electron microscope (SEM) image of CuO_x . Through the image, we can observe that CuO_x forms a thin film with uniform particle size on the BHJ surface.^[41] A complete IPSC cross-section SEM image is shown in Figure S3 (Supporting Information). SnO_2 (20 nm) was deposited on top of FTO as an electron transport layer. Perovskite film (430 nm) was deposited on top of SnO_2 as active layer. BHJ film (76 nm) was deposited on top of perovskite as multisource active layer. CuO_x (57 nm) and Spiro-OMeTAD (176 nm) act as double-HTL to transport photogenerated holes. Ag electrode (110 nm) was deposited on top of Spiro-OMeTAD. The BPQDs fabricated by ultrasonic peeling were characterized by the Raman spectroscopy. As displayed in Figure 2e, three vibrational peaks are ascribed to one out-of-plane phonon mode (A_g^1) at 359.5 cm^{-1} as well as two in-plane modes, B_g^2 and A_g^2 , at 436.0 and 463.3 cm^{-1} , respectively. Compared to bulk BP, the A_g^1 , B_g^2 , and A_g^2 modes of the BPQDs red-shift by ≈ 1.6 , 2.8 , and 2.2 cm^{-1} , respectively. This indicates that the bulk BP has been stripped

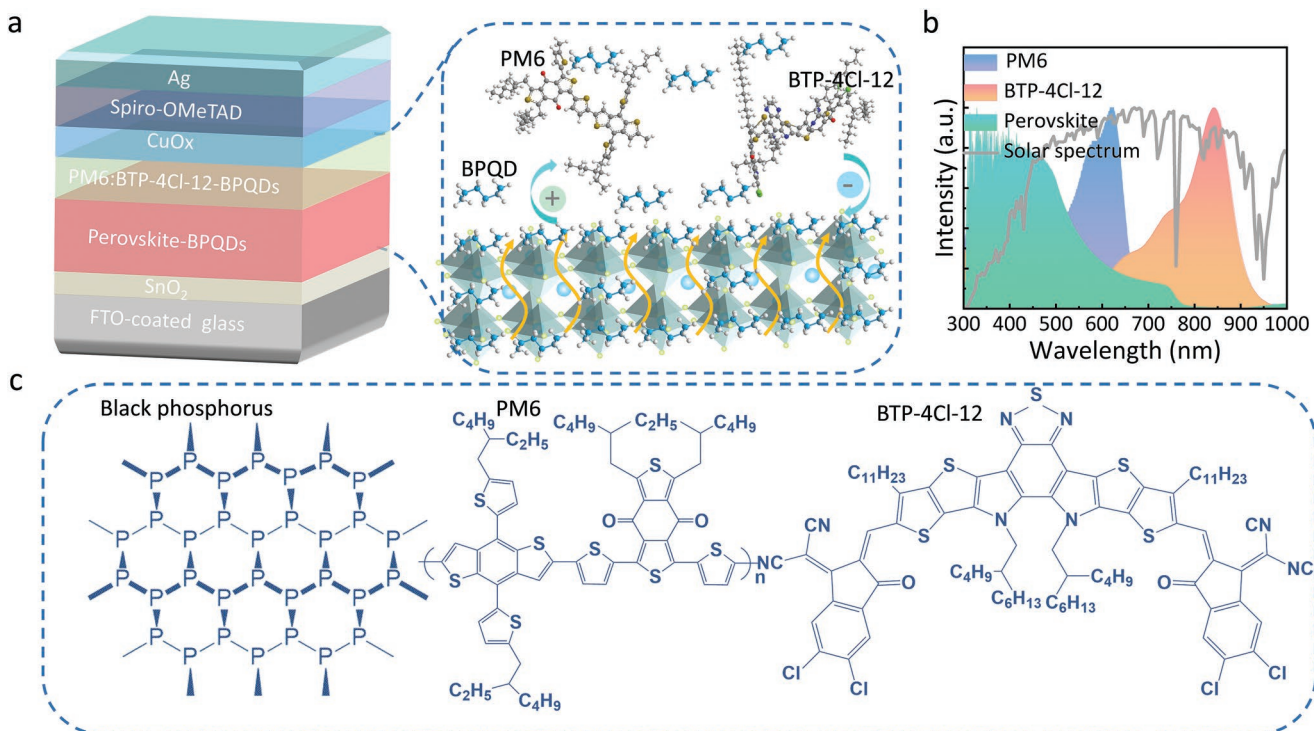


Figure 1. a) Schematic of the optimal IPSC structure. b) Perovskite film PM6 film BTP-4Cl-12 film normalized extinction spectrum and AM1.5G solar energy spectrum. c) Chemical structure of black phosphorus, PM6 and BTP-4Cl-12.

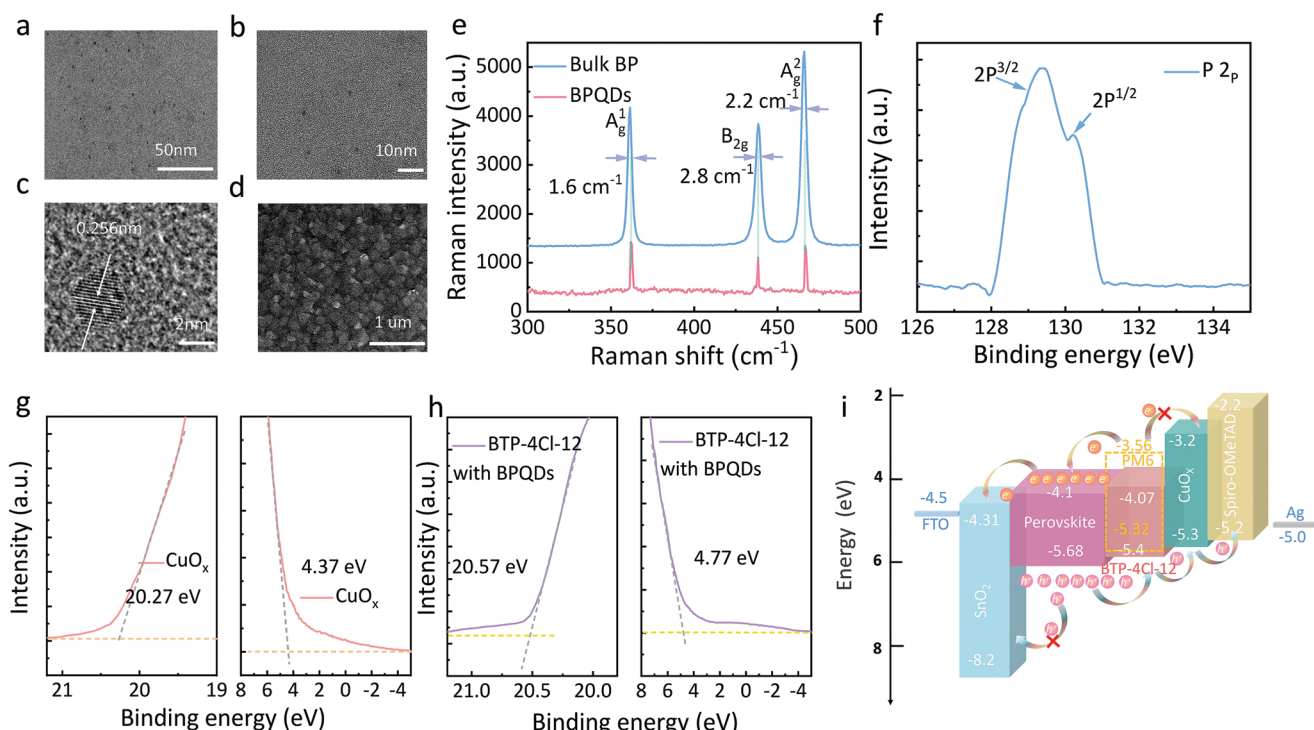


Figure 2. a) TEM image of BPQDs. b) Magnified TEM image. c) HRTEM image of BPQDs. d) top-view SEM image of CuO_x thin film. e) Raman spectra of bulk BP and BPQDs. f) XPS spectrum of BPQDs. g,h) UPS spectrum of BPQDs doped BTP-4Cl-12 film and CuO_x film. i) Energy level distribution diagram of each layer of IPSC device.

into a few layers of BPQDs. The X-ray photoelectron spectroscopy (XPS) results of the manufactured BPQDs (Figure 2f) shows that there are two continuous characteristic peaks at 129.3 and 130.2 eV, which correspond to the $2P^{3/2}$ and $2P^{1/2}$ double peaks of the BP crystal. The ultraviolet photoelectron spectroscopy (UPS) test was performed to determine the work function and the maximum value (V_{max}), highest occupied molecular orbitals (HOMO) of the valence band of CuO_x film, BPQDs doped BTP-4Cl-12 film and BPQDs doped PM6 film (Figure 2g,h and Figure S4, Supporting Information). According to the UPS results, HOMO of BPQDs doped BTP-4Cl-12 film, BPQDs doped PM6 film and V_{max} of CuO_x are calculated to be -5.40, -5.32, and -5.30 eV, respectively. As shown in Figure S5 (Supporting Information), the UPS results of perovskite film show that the position of valence band is almost unchanged. This indicates that a small amount of BPQDs doping did not affect the perovskite lattice and Fermi level. The minimum conduction band lowest unoccupied molecular orbitals (LUMO) of the BTP-4Cl-12 was determined to be 4.07 eV by ultraviolet/visible-near-infrared absorbance spectroscopy (Figure S6, Supporting Information). Based on the above results, the internal energy level distribution of IPSCs device is concluded as shown in Figure 2i. The LOMO energy level of the BHJ is lower than the conduction band minimum (C_{min}) of the hole transport layer and higher than the C_{min} of the perovskite layer and the electron transport layer. This proves that the photogenerated electrons generated by BHJ can be effectively transported to ETL and block the reverse transport of electrons to HTL. The HOMO energy level of the BHJ layer is higher than that of the perovskite layer and lower than the V_{max} of HTL, which proves that the holes from the perovskite and BHJ can be effectively transported to HTL. The HOMO and LOMO of organic materials in IPSC form a good energy level arrangement with the C_{min} band and V_{max} band of inorganic materials. This provides a good driving force for the transport of electrons/holes and suppresses the reverse flow of electrons/holes. The introduction of BPQDs improves the electron/hole mobility of the perovskite/BHJ film and promotes exciton separation, which reduces the recombination of electron-hole pairs that occur at the interface of perovskite film and BHJ film. and improves the overall electrical performance of the IPSCs.

Three kinds devices with structures of, FTO/SnO₂/perovskite/ CuO_x /Ag (Device 1), FTO/SnO₂/perovskite/Spiro-OMeTAD/Ag (Device 2), and FTO/SnO₂/perovskite/ CuO_x /Spiro-OMeTAD/Ag (Device 3), were fabricated. We first explored the effect of different deposition pressures on device performance (Figure S7 and Table S1, Supporting Information). Under the deposition oxygen pressure of 1.57×10^{-1} Pa, device with CuO_x film displays the best performance. Then, the effect of different CuO_x thicknesses on device performance was explored based on the CuO_x and CuO_x /Spiro-OMeTAD, respectively (Tables S2–S4, Supporting Information). Figure 3a shows the J - V curves of the champion devices with the optimized HTL (CuO_x , Spiro-OMeTAD and CuO_x /Spiro-OMeTAD) thickness, respectively. For the PSC device with only CuO_x as the HTL, the champion PCE is 18.23%. J_{sc} , V_{oc} and FF parameters are 21.65 mA cm⁻², 1.138 V and 74.02%, respectively. Table S2 (Supporting Information) lists the influence of CuO_x thickness in Device 1 on the electrical performance of the device. In con-

trast, the PCE of Device 2 (with Spiro-OMeTAD as HTL) and Device 3 (double HTL CuO_x /Spiro-OMeTAD) reach 20.05% and 20.85% (Tables S3 and S4, Supporting Information). The main reason for the PCE increase in Device 3 is resulted from the increase of V_{oc} . The incident photon-to-current-conversion efficiency (IPCE) spectra of the PSCs based on the three champion devices are displayed in Figure 3b. The Device 3 with double HTL exhibits better IPCE than Device 1 and Device 2 in the complete visible wavelength range (300–800 nm). The integrated J_{sc} corresponding to the three champion devices are 21.59, 22.95, and 23.28 mA cm⁻², respectively, which are consistent with the J - V scan results. More than 50 PSCs were prepared to check the repeatability of devices based on different HTLs (Figure 3c and Figure S8, Supporting Information). The average PCE of the three devices is 17.85%, 19.86%, and 20.65%, respectively. The PCE of Device 3 is more concentrated around the average value than Device 1 and Device 2, demonstrating that the double HTL modified device has better repeatability.

In order to get insights on the performance enhancement of devices with different HTLs, we conducted steady-state photoluminescence (PL) based on glass/perovskite/ CuO_x (CuO_x), glass/perovskite/Spiro-OMeTAD (Spiro-OMeTAD), glass/perovskite/ CuO_x /Spiro-OMeTAD (CuO_x /Spiro-OMeTAD). It is widely observed that the introduction of the interface layer with good selective contact can reduce the accumulation of photogenerated carriers between the interface layers. The sample with the CuO_x /Spiro-OMeTAD double HTL (Figure 3d) shows faster fluorescence quenching. Two reasons attribute to the fluorescence quenching of this structure: 1) The extraction rate of photogenerated holes between the perovskite and the double HTL interface is increased. The photogenerated holes are extracted before radiation recombination occurs. 2) The perovskite/double HTL interface undergoes degraded nonradiative recombination, which causes the photogenerated holes to be trapped by the interface defect before radiation recombination. In order to further explore the origin of fluorescence quenching, we performed electrochemical impedance spectroscopy (EIS) in RC mode as displayed in Figure 3e. EIS in RC mode can characterize the nonradiative recombination change of the interface between perovskite and double HTL. The corresponding interfacial recombination impedances of devices prepared based on different HTLs are 526, 810, and 1109 Ω cm⁻², respectively. The increase in interface recombination resistance indicates that the dual HTL suppresses the nonradiative recombination that occurs at the perovskite/HTL interface. The comprehensive evaluation results of PL fluorescence kinetics and EIS show that double HTL accelerates the extraction of photogenerated holes. Fast carrier extraction can ameliorate device V_{oc} , J_{sc} , and FF. The hole transport performance of HTL is an important feature in PSC. To further explore the reasons for the improvement of PSC hole extraction capacity by different HTLs, both hole mobility and hole conductivity were examined by executing space-charge-limited current (SCLC) (Figure 3f) and the two-contact conductivity measurements (Figure 3 g).^[42,43] Hole mobility is evaluated by

$$J = \frac{9}{8} \epsilon_0 \epsilon_r \mu_h \frac{V^2}{L} \quad (1)$$

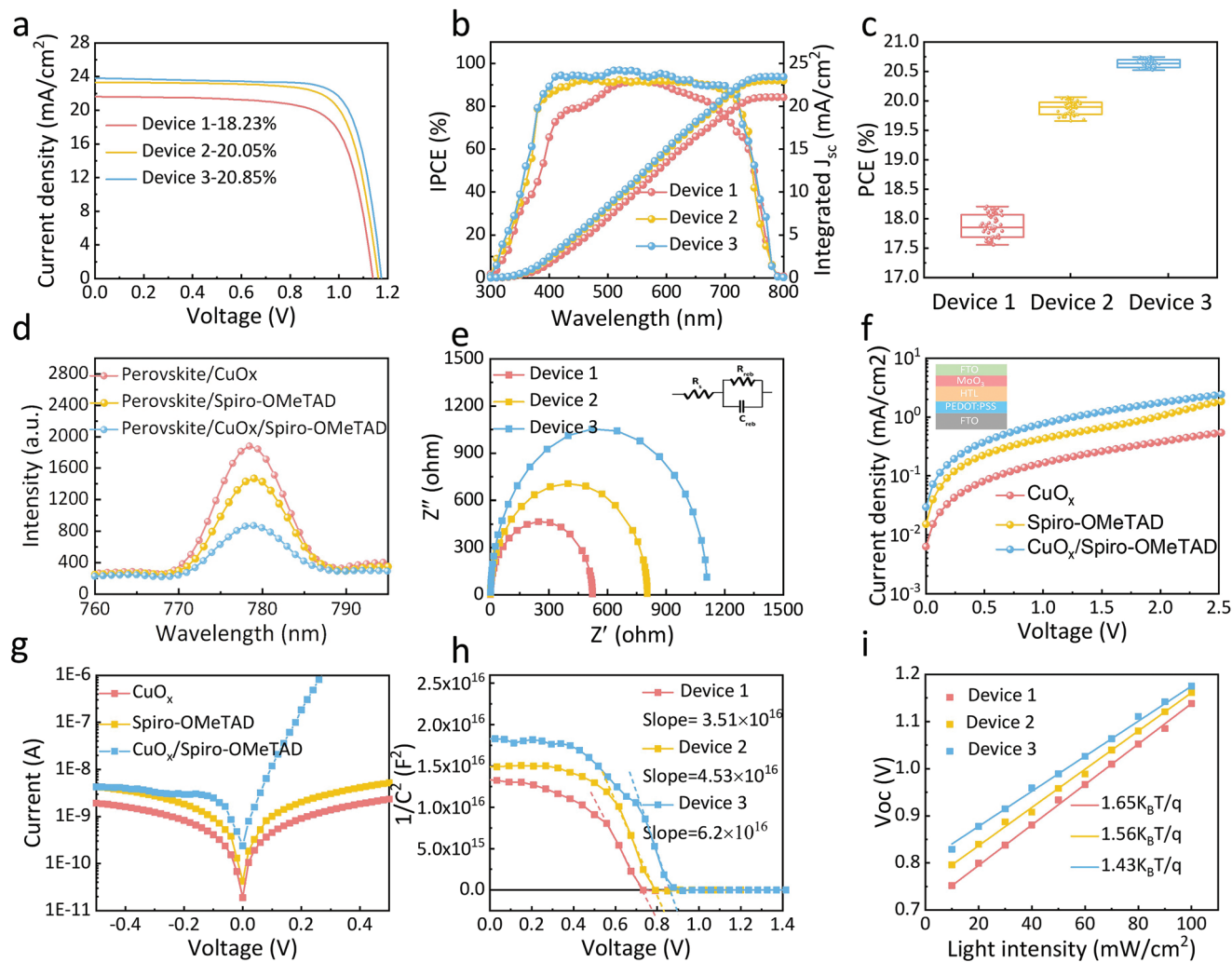


Figure 3. a) Champion J–V curves of FTO/SnO₂/perovskite/CuO_x/Ag (Device 1), FTO/SnO₂/perovskite/Spiro-OMeTAD/Ag (Device 2), and FTO/SnO₂/perovskite/CuO_x/Spiro-OMeTAD/Ag (Device 3) under the AM 1.5 G simulated sunlight illumination (100 mW cm⁻²). b) IPCE curves of FTO/SnO₂/perovskite/CuO_x/Ag (Device 1), FTO/SnO₂/perovskite/Spiro-OMeTAD/Ag (Device 2), and FTO/SnO₂/perovskite/CuO_x/Spiro-OMeTAD/Ag (Device 3). c) Statistical deviation of champion devices based on FTO/SnO₂/perovskite/CuO_x/Ag (Device 1), FTO/SnO₂/perovskite/Spiro-OMeTAD/Ag (Device 2), and FTO/SnO₂/perovskite/CuO_x/Spiro-OMeTAD/Ag (Device 3) structure. d) PL based on glass/perovskite/CuO_x, glass/perovskite/Spiro-OMeTAD, glass/perovskite/CuOx/Spiro-OMeTAD structure. e) EIS of the champion devices based on FTO/SnO₂/perovskite/CuO_x/Ag (Device 1), FTO/SnO₂/perovskite/Spiro-OMeTAD/Ag (Device 2), and FTO/SnO₂/perovskite/CuO_x/Spiro-OMeTAD/Ag (Device 3) structure. Inset shows the equivalent circuit model employed for the fitting of the impedance spectra. f) Hole mobility measurements using space-charge limited currents for the HTLs CuO_x, Spiro-OMeTAD, and CuO_x/Spiro-OMeTAD (Inset shows the structural model used to evaluate the SCLC). g) J–V characteristics of the HTLs CuO_x, Spiro-OMeTAD, and CuO_x/Spiro-OMeTAD recorded under dark conditions. h) MS plots of the champion devices with different HTL. i) Plots of V_{oc} as a function of the light intensity of Device 1, Device 2, and Device 3.

where J is the current density in the dark, ϵ_0 is the permittivity of free space (8.85×10^{-12} F m⁻¹), ϵ_r is the dielectric constant of the semiconductor material, μ_h is the hole mobility, V is the applied voltage, and L is the thickness of the active layer. Hole conductivity can be evaluated by

$$\sigma = pq\mu_p \quad (2)$$

where σ is the hole conductivity, p is the hole density, q is the charge quantity, μ_p is hole mobility. The result indicates that double HTL shows a higher mobility

(2.95×10^{-4} cm² V⁻¹ s⁻¹), than CuO_x (0.32×10^{-4} cm² V⁻¹ s⁻¹) and Spiro-OMeTAD (1.28×10^{-4} cm² V⁻¹ s⁻¹). As expected, the hole conductivities of different HTLs are double-HTL (2.52×10^{-4} S/cm), CuO_x (2.74×10^{-5} S/cm), Spiro-OMeTAD (1.097×10^{-4} S/cm), respectively. The higher mobility of double-HTL is favorable for enhancing charge extraction, resulting in higher J_{sc} , V_{oc} , and FF in the solar cell devices. The built-in potential (ϕ_{bi}) is an important indicator to understand the physical characteristics of the device. It directly affects the distribution of the internal electric field. Mott–Schottky (MS) of different HTL devices is executed to evaluate ϕ_{bi} . The MS

plots corresponding to different HTL devices are shown in Figure 3h.^[44] The relationship between capacitance and voltage is evaluated by

$$\frac{1}{C^2} = \frac{2}{A^2 q \epsilon_0 \epsilon N} \left(\varphi_{bi} - V - \frac{2KT}{q} \right) \quad (3)$$

where C is the capacitance of the Schottky contact, A is the active area, q is the elementary charge, ϵ_0 is the vacuum permittivity, ϵ is the relative permittivity of the material, N is the concentration of the charged defects, φ_{bi} is the built-in potential, and V is the applied voltage. The built-in voltage can be obtained from the intersect with the voltage axis in the $1/C^2$ versus V curves. MS detection results show that the double HTL has a larger intercept at $1/C^2 = 0$, which shows that the inclusion of CuO_x in the device adjusts the energy level structure and improves the built-in potential. The improvement of the φ_{bi} is one of the direct factors to increase the V_{oc} of the device. The N value of the function relationship between V_{oc} and light intensity can evaluate the carrier recombination outside the depletion layer. The N value corresponding to different HTL devices is shown in Figure 3i. Compared with Device 1, the N value of Device 3 with double HTL is reduced from 1.65 to 1.43, which proves that the dual HTL suppresses the carrier recombination that occurs outside the high barrier region.

Based on the above-mentioned research on dual HTL devices, we further fabricated IPSC with excellent infrared response ability. In the IPSC part, we fabricated devices with four structures: FTO/SnO₂/perovskite/CuO_x/Spiro-OMeTAD/Ag (S1), FTO/SnO₂/perovskite/BHJ/CuO_x/Spiro-OMeTAD/Ag (S2), FTO/SnO₂/perovskite-BPQDs/BHJ/CuO_x/Spiro-OMeTAD/Ag

(S3) and FTO/SnO₂/perovskite-BPQDs/BHJ-BPQDs/CuO_x/Spiro-OMeTAD/Ag (S4). The champion devices with different structure are displayed in Figure 4a (the detailed $J-V$ performance are shown in Tables S5-S8, Supporting Information). The Device S2 with BHJ has a higher J_{sc} than the control device S1, indicating BHJ in the PSC have a gain effect on J_{sc} . But a certain degree of loss in V_{oc} can be observed for device S2, which is induced by the introduction of BHJ. After introducing BPQDs into perovskite layer (Device S3), the J_{sc} , V_{oc} , and FF display a considerable improvement. Further employing BPQDs in BHJ (Device S4), the J_{sc} and V_{oc} continue to increase. The PCE of the champion device (S4) reaches 23.52% with $J_{sc} = 25.22 \text{ mA cm}^{-2}$, $V_{oc} = 1.162 \text{ V}$ and FF = 80.27%. Figures 4b and 4c show the distribution diagram of electrical parameters for different devices. The PCE improvement of S2, S3, S4 is mainly derived from the improvement of V_{oc} , J_{sc} , and FF. The introduction of BPQD solves the problem of a large V_{oc} loss caused by BHJ, which plays a significant role on enhancing the performance of IPSCs. BP materials with different dimensions also have a certain influence on the performance of the device. To investigate this effect, we measured the performance of the modified IPSCs with different concentrations of BP nanosheets (Figure S9, Tables S9 and S10, Supporting Information). The champion device decorated with BP nanosheets obtained a PCE of 22.73%, which is lower than the performance of BPQD-modified champion devices. Then we evaluated the IPCE of S1, S2, S3 and S4 devices as shown in Figure 4d. S1 demonstrates the light response cut off at 800 nm. After introducing BHJ, device S2 exhibits excellent infrared response ability, with maximum IPCE value of 47%. But the light response value at the visible light region decreases to a certain extent. We

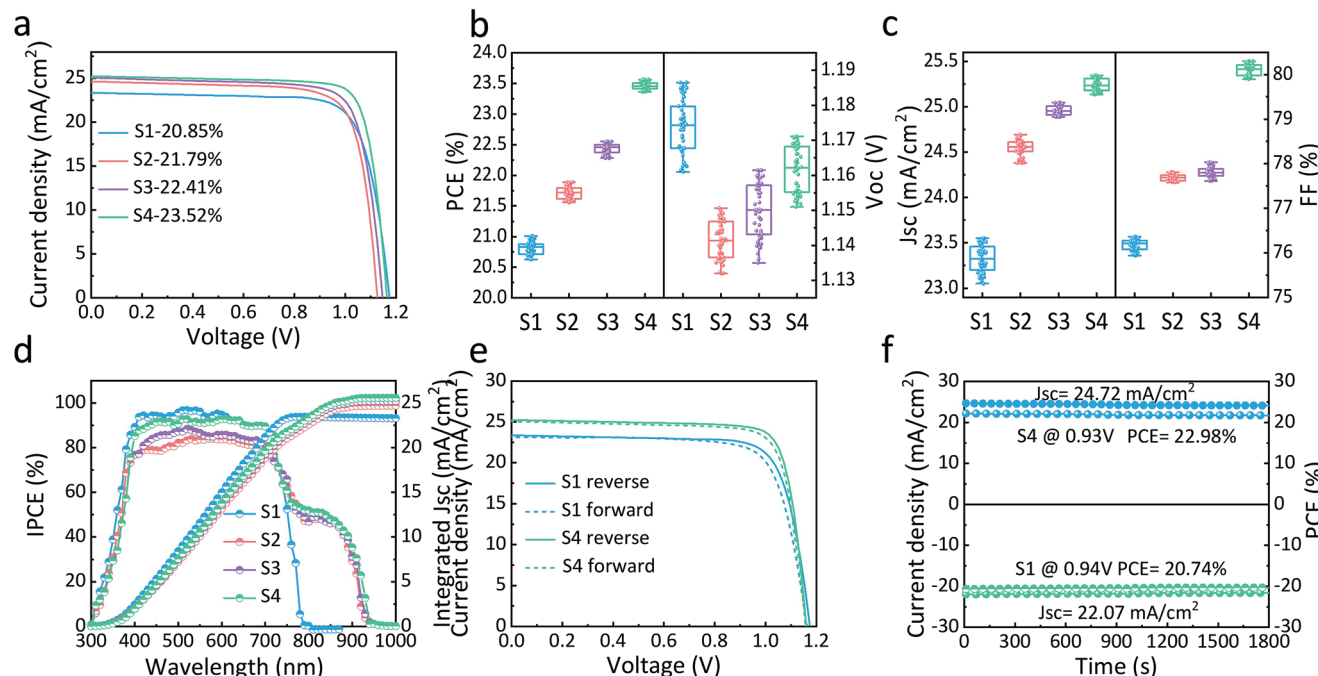


Figure 4. a) The $J-V$ characteristic curves of the S1, S2, S3, S4 device. b,c) Statistical deviation of the photovoltaic parameters of S1, S2, S3 and S4 device. d) The IPCE curves of the S1, S2, S3, S4 device. e) $J-V$ curves for S1, S4 device under forward and reverse scans. f) Steady-state output power of S1 and S4 champion devices.

speculate that this phenomenon is caused by the recombination of carriers that occurs inside and at the interface of the perovskite/BHJ film. After introducing BPQDs into the device (S3 and S4), the improved IPCE value in the visible and infrared regions indicates the carrier recombination at the interface of perovskite and BHJ layers is inhibited to some extent. Particularly, the maximum IPCE value at infrared region reaches 51%. The J_{sc} calculated by the IPCE curve is 23.28, 24.56, 24.97, 25.19 mA cm⁻², respectively, which is consistent with the results obtained by $J-V$. Figure 4e and Table S11 (Supporting Information) show the hysteresis curves of S1 and S4. The $I-V$ reverse scan of the device S4 is 23.52%, and the forward scan is 23.03%, the hysteresis factor of which is reduced from 0.027 to 0.021 compared with device S1. The steady-state photocurrent output was performed under the maximum power point (MPP) bias to confirm the reliability of the device. As shown in Figure 4f, the optimal S4 maintains a stable PCE of 22.98% and photocurrent of 24.72 mA cm⁻² after 1800s, while device S1 exhibits a slight decline. This indicates that the optimized device has good light stability.^[45,46]

It is an effective method to directly deposit BHJ with infrared absorption capability on top of the perovskite film to expand the infrared absorption capability of PSC. In IPSC devices, although the low band gap BHJ can harvest infrared light to enhance the photocurrent, the interface nonradiative recombination generated by the perovskite/BHJ interface can cause the loss of the device surface photovoltage and FF. Table 1 lists the recent development of the representative application of BHJ materials in PSCs. Many researchers have achieved excellent results. For example, A. K. Jen and Zhu et al. introduced PM6: CH1007 into PSC and achieved a highest PCE of 23.8%. In their work, the PCE of the control device based on PCBM FTL is 22.44, which makes it more competitive in the photovoltaic field. Although the IPSC device successfully achieved the highest PCE of 23.8%, the maximum photoresponse from CH1007 is limited to below 20% and the photocurrent response contribution value of the device in the near-infrared region was only 5% and there was a certain degree of FF loss. In this work, we adjust the carrier transport of perovskite and BHJ through BPQDs and CuO_x achieving the champion device with a PCE of 23.52%. IPSC device achieved 51% maximum light response value in the infrared region with infrared photocurrent contribution of 16.5% and a higher short-circuit current density without sac-

rificing V_{oc} and FF. This work demonstrates an approach to solve the carrier extraction issues that limits the performance of IPSCs, which overcomes the bottleneck of IPSCs. It makes this work an instructive result and at the top level in the IPSC field.^[8,9,11,47–51] We believe that if the PCE of our control devices is further improved, the highest IPSC PCE will be obtained.

To understand the mechanism of the improvement induced by the BHJ and BPQDs, a series of optoelectronic tests were executed. First, we explored the mechanism of performance improvement induced by BHJ in PSC device. BHJ and perovskite have complementary characteristics of light response. The photoelectric response range of S2 device with BHJ has been broadened to 930 nm and the maximum response value in the range of 800–960 nm can reach 47% (Figure S10, Supporting Information). The wide photoelectric response range enhances the photocurrent of the device, which directly lead to enhancement PCE of S2. XPS measurement was executed to examine the passivation effect of BHJ on perovskite film, as shown in Figure 5a (During the XPS test, we spin-coated the ultra-low concentration BHJ solution on the surface of the perovskite film to prepare an extremely thin BHJ film). The binding energy of O 1s in the perovskite/BHJ film is 532.67 eV, which shows an increase of 0.82 and 0.68 eV compared to that of pure perovskite film (531.85 eV) and BHJ film (531.99 eV), respectively. This can be attributed that the additional Coulomb force interaction between the photogenerated electrons and the charged ion nucleus causes a higher oxidation state. The additional Coulomb force could come from Pb–O. As shown in Figure S11 (Supporting Information), the binding energy of Pb 4f in perovskite/BHJ film shows a peak shift of 0.5 eV compared to the pure perovskite film. The increase of Pb binding energy indicates that the Pb⁰ defects existing on the surface of the perovskite are oxidized and eliminated. The extra Pb is consumed through combining with O element in BHJ. Therefore, BHJ can not only provide the additional light response at the infrared region, but also display the surface passivation to form the high-quality perovskite film, which is the fundamental reason for the performance improvement of S2 device.

In order to understand the influence of BPQDs on the internal electrical properties of the perovskite film and BHJ film, the current-voltage curve in the dark state was executed. Figure 5b and Figure S12 (Supporting Information) shows the dark current–voltage curves of representative pristine and

Table 1. A summary of recent development of the representative application of BHJ materials in PSCs.

| BHJ materials | Device structure | V_{oc} [V] | FF [%] | J_{sc} [mA cm ⁻²] | ΔJ_{sc} [mA cm ⁻²] | PCE [%] | Ref. |
|-----------------------------|------------------|--------------|--------|---------------------------------|--|---------|-----------|
| TT:N2200 | p-i-n | 1.1 | 73 | 22.05 | 2.18 | 17.7 | [11] |
| PDTP-DFBT | p-i-n | 0.96 | 78 | 21.1 | 1.6 | 15.8 | [50] |
| PBDB-TF:BTP-4Cl | n-i-p | 1.09 | 79 | 25.02 | 3.27 | 21.55 | [51] |
| PBDB-T:BT2b-Rc | n-i-p | 1.22 | 72.66 | 12.5 | 2.32 | 11.08 | [9] |
| PM6:CH1007 | p-i-n | 1.146 | 79.67 | 26.07 | 1.25 | 23.8 | [47] |
| IEICO-4F | n-i-p | 1.14 | 76 | 24.9 | 1.3 | 21.6 | [8] |
| Y6 | p-i-n | 1.12 | 79 | 23.68 | 1.04 | 21.0 | [48] |
| S1:Y6 | p-i-n | 1.09 | 67.3 | 28.06 | 5.54 | 20.61 | [49] |
| PM6:BTP-4Cl-12 (with BPQDs) | n-i-p | 1.162 | 80.27 | 25.22 | 3.57 | 23.52 | This work |

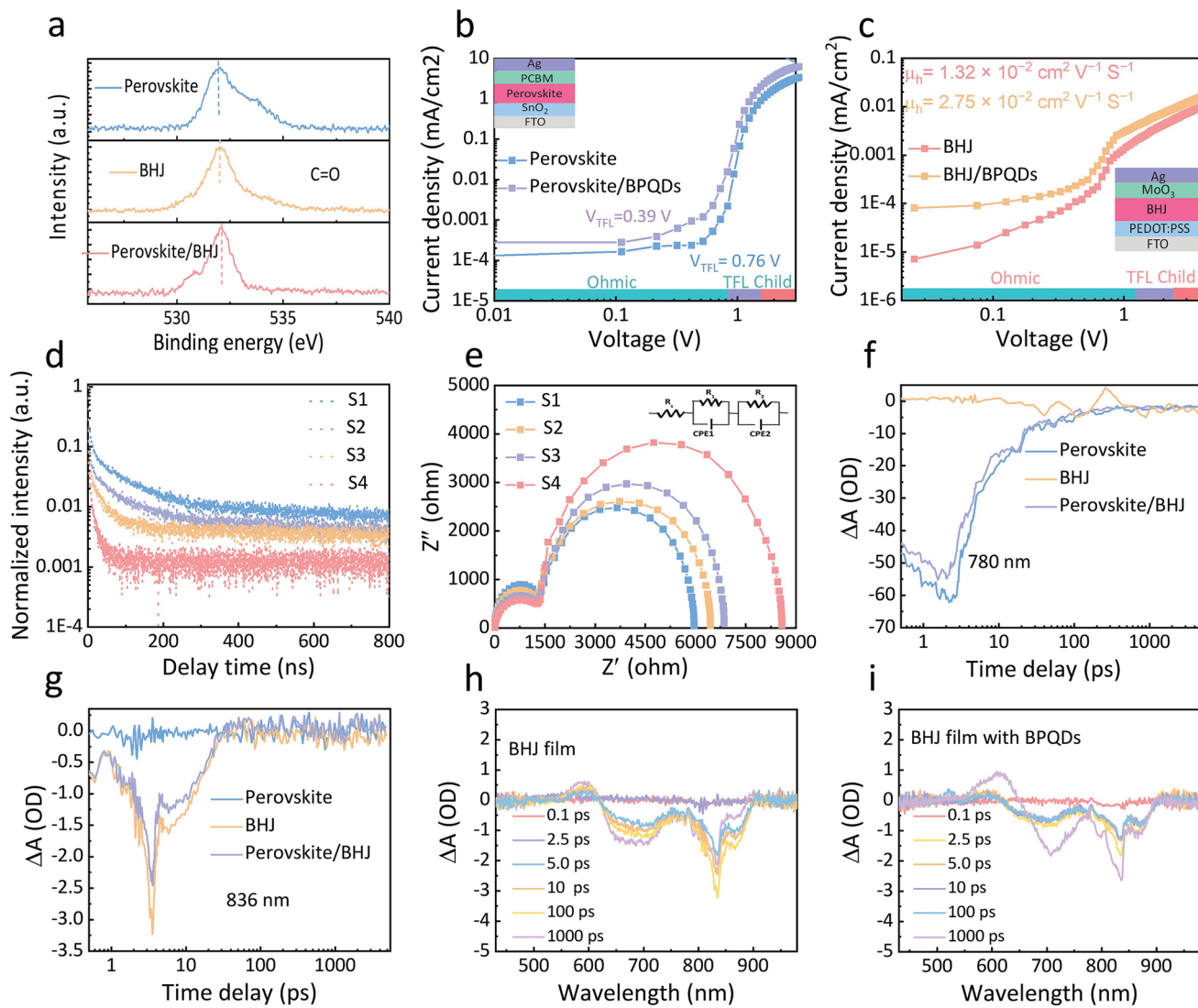


Figure 5. a) O 1S XPS of perovskite film, BHJ film, perovskite/BHJ film. b) Dark current–voltage (I – V) characteristics of electron-only devices based with FAMA perovskite films without and with BPQDs. c) Dark current–voltage (I – V) characteristics of hole-only devices based with BHJ films without and with BPQDs. d) TRPL spectra of S1, S2, S3, S4 devices. e) Nyquist plots of S1, S2, S3, S4 device measured in the dark under a reverse potential of 1.0 V. Inset shows the equivalent circuit model employed for the fitting of the impedance spectra. f) uTAS measurement of perovskite film, BHJ film and perovskite/BHJ film with excitation at 410 nm. The excited charge carriers in perovskite, BHJ and perovskite/BHJ are probed at a laser wavelength of 780 nm. g) uTAS measurement of perovskite film, BHJ film and perovskite/BHJ film with excitation at 410 nm. The excited charge carriers in perovskite, BHJ and perovskite/BHJ are probed at a laser wavelength of 836 nm. h) uTAS measurement of BHJ film. i) uTAS measurement of BHJ film with BPQDs.

BPQDs-containing electron-only perovskite devices and hole-only perovskite devices. They both exhibit a linear Ohmic response at low bias, a trap-filled limit regime, and a trap-free space-charge limited current (SCLC) regime. The defect state density is determined by the following formula

$$N_t = \frac{2\epsilon_0\epsilon_r V_{TFL}}{qL^2} \quad (4)$$

where ϵ_0 is the vacuum permittivity, ϵ_r is the relative dielectric constant, V_{TFL} is the onset voltage of the trap-filled limit region, q is the elemental charge, and L is the thickness of the film. It can be observed that the defect state densities are $(1.28 \pm 0.28) \times 10^{16} \text{ cm}^{-3}$ for the pristine FAMA device and

$(2.52 \pm 0.11) \times 10^{15} \text{ cm}^{-3}$ for the BPQDs modified FAMA devices, respectively. The electron mobility of the perovskite film with BPQDs and the pure perovskite film is calculated by formula 1 as $8.42 \times 10^{-2} \text{ cm}^2 \text{ V}^{-1} \text{ s}^{-1}$ and $5.95 \times 10^{-2} \text{ cm}^2 \text{ V}^{-1} \text{ s}^{-1}$, respectively. The hole mobility of the perovskite film with and without BPQDs are $0.82 \times 10^{-2} \text{ cm}^2 \text{ V}^{-1} \text{ s}^{-1}$ and $0.35 \times 10^{-2} \text{ cm}^2 \text{ V}^{-1} \text{ s}^{-1}$, respectively (the detail performance of the carrier mobility is displayed in Table S12, Supporting Information). The increased carrier mobility demonstrates that BPQDs improves the charge carrier transport capacity of the perovskite layer, which accelerates the extraction of electrons at the interface between the perovskite layer and the BHJ layer. The reduced density of defect states indicates that the trapping ability of the internal

defects of the perovskite layer to charge carriers is weakened, which reduces the nonradiative recombination of photo-generated carriers that occurs inside the perovskite film. We performed $J-V$ curve test with hole-only and electron-only structure in the dark state to evaluate the effect of BPQDs on the BHJ defect state and hole mobility (Figure 5c and Figure S13, Supporting Information). The hole mobility of BHJ and BHJ with BPQDs calculated by formula (1) are 1.32×10^{-2} , $2.75 \times 10^{-2} \text{ cm}^2 \text{ V}^{-1} \text{ S}^{-1}$ respectively. In contrast, the hole mobility of the BHJ with BPQDs device is approximately twice of that in BHJ device. At the same time, the electron mobility of BHJ and BHJ with BPQDs calculated by formula (1) are 7.26×10^{-3} , $0.26 \times 10^{-2} \text{ cm}^2 \text{ V}^{-1} \text{ S}^{-1}$, respectively. This indicates that BPQDs can effectively enhance the hole and electron transport capacity of BHJ layer and exciton separation within BHJ. The increased carrier mobility accelerates the extraction of hole at the interface between the perovskite layer and the BHJ layer. The holes are extracted before the interface recombination. At the same time, the suitable energy levels arrangement of the BHJ and the perovskite layer not only hinder the reverse flow of electrons and holes, but also make electron/hole smoothly transported to the cathode/anode under the drive of the built-in electric field. BPQDs improve the carrier transport inside the device. This is the most direct reason for the increase in V_{oc} of S3 and S4 devices. In order to understand the type of compounding mechanism, as shown in Figure S14 (Supporting Information), we the ideality factor N by plotting V_{oc} as a function of light intensity. The ideality factors obtained from the linear fitting of the plot are 1.43 (S1), 1.37 (S2), 1.26 (S3), 1.11 (S4), respectively. The value of n, which obtains from the image is in the range of $1 \ll n \ll 2$. It indicates that trap-assisted Shockley-Read-Hall (SRH) recombination is the main type of recombination process. When BPQD is introduced into the perovskite and BHJ, the trap densities within the bulk together with the interfacial traps decrease.^[52,53] Based on glass/perovskite/CuO_x/Spiro-OMeTAD (S1), glass/perovskite/BHJ/CuO_x/Spiro-OMeTAD (S2), glass/perovskite-BPQDs/BHJ/CuO_x/Spiro-OMeTAD (S3), glass/perovskite-BPQDs/BHJ-BPQDs/CuO_x/Spiro-OMeTAD (S4) structure, we tested PL and Time-resolved photoluminescence spectra (TRPL) to explore the influence of BHJ and BPQDs on the interface carrier dynamics of the device. As shown in Figure S15 (Supporting Information) the devices modified with BHJ and BPQDs have a certain degree of fluorescence quenching compared to S1. Two reasons lead to PL quenching: (1) the increased carrier extraction rate between the perovskite/BHJ interfaces; (2) deteriorating nonradiative recombination between perovskite/BHJ interfaces. TRPL measurements further provide similar results, showing biexponential decay of fast and slow components (Figure 5d and Table S13, Supporting Information). The fast decay component (τ_1) mainly represents the nonradiative recombination induced by trap states at grain boundaries and surfaces while the slow decay component (τ_2) is assigned to the free carrier recombination (radiative recombination). The decrease in τ_1 component suggests that S2 (35.46 ns), S3 (15.40 ns), S4 (12.14 ns) device injects photogenerated holes into HTL faster than the S1 device (37.80 ns), indicating an enhancement of the charge extraction process at the corresponding interface. This should be attributed to the minimum interface trap state and the excellent hole

transfer ability between the interfaces after BPQDs modification. As shown in Figure 5e, EIS with a frequency of 0.1 Hz–10⁵ kHz was performed to explore the charge transfer behavior of these devices. The arc at high frequency is the characteristic of carrier transport, and the semicircle at low frequency is the result of carrier recombination. According to the equivalent circuit, the values of interfacial recombination resistance (R_{rec}) and charge transfer resistance (R_{ct}) are fitted. For the control device S1, R_{ct} is 795 Ω and R_{rec} is 5958 Ω. The modified devices S2, S3, and S4 exhibited lower R_{ct} (686 vs 591 vs 502 Ω) and higher R_{rec} (6502 vs 6856 vs 8581 Ω), indicating the generated carriers can be transported efficiently after integrated with HTL and BPQDs. To further explore the effect of BPQDs on the carrier dynamics of perovskite and BHJ films, we performed ultrafast transient absorption spectroscopy (uf-TAS) measurement. As shown in Figure 5f, by examining the ground-state bleaching and stimulated emission signals of perovskite thin films, we found that there is a slightly faster decay of the perovskite bleach kinetics after its direct excitation by 410 nm in the perovskite/BHJ film compared with the perovskite film. Correspondingly, the faster decay of BHJ bleach kinetics is also observed in perovskite/BHJ film compared with the single BHJ film (Figure 5g). These results indicate the efficient charge-transfer occurs at the interfaces of perovskite and BHJ films. As shown in Figure 5h,i, we used a 410 nm excitation source to explore the optical density changes of BHJ films before and after doping with BPQDs. We found that the bleach bands of BHJ film with BPQDs decay faster compared with the single BHJ film, which indicates the more efficient carrier extraction after introducing BPQDs. Meanwhile, the bleach kinetics of perovskite/BHJ film decays slightly faster after introducing BPQDs in perovskite and BHJ films (Figure S16, Supporting Information). These results indicate that the electrons and holes at the interfaces of BHJ and perovskite layers can be efficiently extracted due to the existence of high-mobility BPQDs in the perovskite and BHJ film. The presence of BPQDs weakens the interfacial barrier between the perovskite layer and the BHJ layer and accelerates the carrier transport rate inside the device. This provides additional support for the interfacial charge transfer results detected by TRPL in Figure 5d. These results prove the photocurrent contribution of BHJ film and the enhanced carrier extraction ability enabled by BPQDs. The short-circuit current density-voltage relationship in the dark state of the device was evaluated to determine the carrier recombination outside the depletion layer (Figure S17, Supporting Information). When the intercept voltage is 0 V, the dark current density (J_0) of S1, S2, S3, S4 are 2.13×10^{-7} , 2.26×10^{-8} , 1.86×10^{-9} , $3.72 \times 10^{-10} \text{ mA cm}^{-2}$, respectively. The J_0 of the modified device is largely reduced, indicating that the internal carrier transmission rate of the modified device is much higher.

Based on the above discussions, the mechanism of BPQDs on the charge dynamics behavior of integrated perovskite solar cells can be concluded. Due to the undesirable hole and electron transport characteristics of the BHJ perovskite film, this leads to the accumulation of large number of photo-generated electrons and holes at the interface of the perovskite film and the BHJ film. For the device without BPQDs, electrons and holes are consumed through the recombination

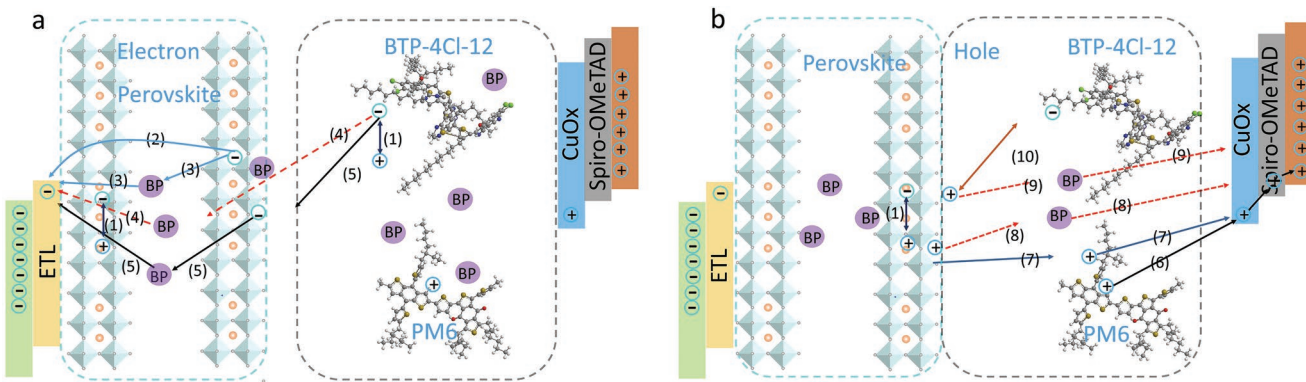


Figure 6. a) The internal electron transport mechanism of the IPSC device after BPQDs are introduced into the IPSC device. b) The internal hole transport mechanism of the IPSC device after BPQDs are introduced into the IPSC device.

at the interface of perovskite film and BHJ film. With the BPQDs doped perovskite and BHJ active layer strategy, BPQDs with high carrier mobility can improve the carrier extraction capability of IPSC devices. A certain amount of BPQDs with high hole/electron mobility were incorporated into perovskite films and BHJ films to enhance the electron/hole transport ability inside perovskite film and BHJ film. The carriers between the perovskite and BHJ interface are extracted before recombination, which effectively inhibits the interface reorganization caused by the accumulation of carriers at the interface of the perovskite film and the BHJ film. The matched energy level inside the IPSC device provides excellent driving force for electrons and holes. P-type CuO_x with excellent hole mobility and matched hole extraction ionization potential, which reduces the carrier recombination between BHJ/HTL. The suppression of interface nonradiative recombination increased the surface photovoltage and FF of the IPSC device, which finally achieved the champion device with a PCE of 23.52%. Figure 6a,b show the electron and hole transportation process of BPQDs introduced into the IPSC device. The photogenerated electrons and holes can be faster extracted through regulating the carrier transport behaviors at the interfaces of perovskite/BHJ and BHJ/HTL by CuO_x and BPQDs. The photogenerated electrons/holes are effectively transported to the cathode/anode under the drive of the built-in electric field, which is essential for the manufacture of high-performance IPSC.

The stability of solar cell devices is an important indicator for commercial applications. Figure 7a-d are the XRD patterns of the original perovskite film, perovskite-BPQDs, perovskite-BPQDs/BHJ and perovskite-BPQDs/BHJ-BPQDs before and after exposure to environmental conditions.^[54] After exposure for three months, the original perovskite film discolored and scaled from the substrate (inset of Figure 7a), as well as the formation of PbI_2 , owing to the decomposition and hydration of $(\text{FA}_{0.85}\text{MA}_{0.15})\text{Pb}(\text{I}_{0.85}\text{Br}_{0.15})_3$.^[55-58] In contrast, BPQDs and BHJ modified films showed impressive stability after three months of storage under ambient conditions. The film color and phase changed slightly. The unpackaged S1, S2, S3, and S4 devices were placed in a dark atmosphere with a relative humidity of 30% for aging test. As shown in Figure 7e, after 3500 hours of aging, the control device S1 is completely

decomposed, while the S2, S3, and S4 devices can still maintain 62.2%, 67.9%, and 85.2% of the initial efficiency. The reason for this phenomenon is mainly due to the passivation effect of BHJ and BPQDs on the inside and surface of the perovskite film. The phase segregation caused by perovskite grain boundaries and surface defects is an important reason for the decomposition of perovskite active layer.^[59] As shown in Figures 5a, the heterojunction can passivate the surface defects of the active layer of the perovskite and inhibit the phase segregation caused by the defects. In a humid environment, moisture can cause serious degradation of perovskite materials. We evaluated the humidity stability of unencapsulated devices under dark conditions with a relative humidity of $65\% \pm 5\%$. As shown in Figure 7f, the efficiency changes of S1, S2, S3, and S4 devices within 300 hours are periodically collected. S1 is completely decomposed after 300 hours of storage, but the efficiency of S2, S3, S4, and devices after 300 hours are reduced to 71%, 79% and 81% of the initial efficiency.^[60] We have tested the hydrophobic angle of different samples as shown in Figure 7 g. From the test results we can observe that the perovskite film contact angle is 53.295° the perovskite-BPQDs film contact angle is 61.525° the perovskite-BPQDs/BHJ contact angle is 87.71° the perovskite-BPQDs/BHJ-BPQDs contact angle is 92.29° . The increased hydrophobic angle indicates the increased hydrophobic performance of the device.^[61-63] BPQDs can optimize the crystalline quality of the perovskite film and reduce the surface area of the grain boundary in contact with water molecules, which improves the moisture and hydrophobic properties of the perovskite film to a certain extent. Defects at the surface and grain boundaries of perovskite films affect the long-term stability and humidity stability of the device. The grain boundaries of perovskite films consist of amorphous intergranular layers, which allow moisture to diffuse into the perovskite films rapidly. In the process of thermal annealing of perovskite films, a large number of water-sensitive methylamine ions are generated, which plays a crucial role in the stability of perovskite films. The grain boundary density of perovskite films highlights the importance of stabilizing grain boundaries to improve the stability of perovskite solar cells. As shown in Figures S18 and S19 (Supporting Information), the average grain size of BPQDs-modified perovskite films increases from 290 nm to

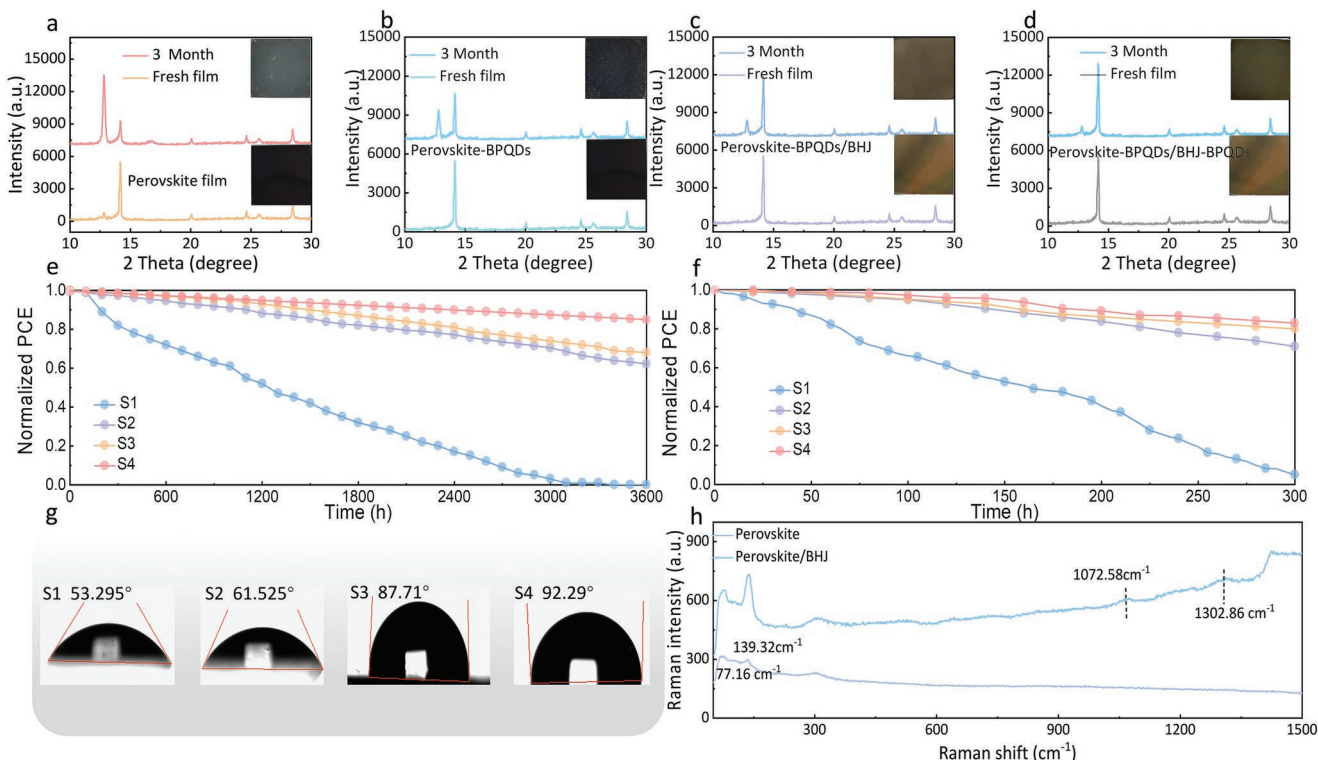


Figure 7. XRD patterns of a) pristine perovskite thin film, b) perovskite-BPQDs thin film, c) perovskite-BPQDs/BHJ thin film, and d) perovskite-BPQDs/BHJ-BPQDs thin films before and after exposure to ambient conditions for three month. Insets: corresponding photographic images of perovskite thin films or perovskite/BHJ thin film. e) Long-term stability of S1, S2, S3, S4 devices. f) Humidity stability of S1, S2, S3, S4 devices. g) Water contact angle of pristine perovskite, perovskite-BPQDs, perovskite-BPQDs/BHJ, perovskite-BPQDs/BHJ-BPQDs thin films. h) Confocal Raman microscopy of perovskite film and perovskite/BHJ film.

420 nm compared to unmodified perovskite films. The grain size of BPQDs-decorated perovskite films becomes significantly larger, which indicates that the BPQDs promote the crystallinity of the perovskite films, which reduces the grain boundary density and the number of water-sensitive methylamine ions. The lower grain boundary density and larger grain size lead to enhanced water resistance of PSCs, which in turn leads to improved long-term stability and humidity stability of the device.^[64,65] In order to further explore the reasons for the change in the hydrophobic angle of the device, confocal Raman microscopy has evaluated the molecular bonds in the material (Figure 7h and Figure S20, Supporting Information). Two vibrational peaks at 77.16 cm⁻¹ and 139.32 cm⁻¹ can be ascribed to perovskite film. The 1095.56 cm⁻¹ and 1316.75 cm⁻¹ vibrational peaks can be ascribed to long-chain aryl groups in BHJ film. After depositing BHJ on the perovskite film, vibration peaks corresponding to the long-chain aryl groups in PM6 and BTP-4Cl-12 appear at 1072.58 cm⁻¹ and 1302.86 cm⁻¹, respectively. The blue-shifted vibration peaks demonstrate that BHJ forms a stronger molecular bond with the surface of the perovskite film. This indicate that the BHJ film passivates the surface defects of the perovskite film and weakens the phase segregation of the perovskite film. The suppression of the perovskite phase segregation will reduce the generation of water-absorbing methylamine ions, which enhances the humidity stability of the device. Long-chain aryl groups have good hydrophobic properties, which is an important factor

for BHJ to increase the hydrophobic properties of the device (Figure S21, Supporting Information).

3. Conclusions

In this work, we tuned the bipolar transport properties of perovskite and BHJ films through the introduction of CuO_x and BPQDs into IPSC. First, we introduced CuO_x to construct a double-HTL structure. Dual HTL has matched energy levels and excellent hole conduction characteristics, which inhibits the nonradiative recombination of the active layer/HTL interface. Then we integrated BHJ with excellent near-infrared absorption capability into PSCs to fabricate an IPSC with a light response range of 930 nm. Bipolar BPQD with excellent mobility was introduced into both perovskite and BHJ films, which enhanced the transport capacity of perovskite and BHJ for electrons and holes in IPSC. This strategy reduced the nonradiative recombination that occurred at the perovskite/BHJ interface and improved the FF and V_{oc} of the IPSC device. Owing to the efficient carrier transport and considerable contribution of NIR response, the 23.52% PCE for the champion IPSC device was obtained. At the same time, the long-term stability and humidity stability of the devices modified by BHJ and BPQDs were greatly enhanced. This work provides an effective strategy to eliminate the serious nonradiative recombination between the perovskite, BHJ and HTL internal and interface

in IPSC, which lays the foundation for the application of high-performance IPSC in the future.

Supporting Information

Supporting Information is available from the Wiley Online Library or from the author.

Acknowledgements

This work was supported by the Key Program of NSFC-Guangdong Joint Funds of China (U1801253), the National Key Research and Development Program (2016YFC0207101), the National Natural Science Foundation of China (Grant Nos. 12174152, 11874181, and 11904124), the Special Project of the Province-University Co-constructing Program of Jilin Province (SXGJXX2017-3), Jilin Province Youth Scientific and Technological Talent Support Project, Interdisciplinary Integration and Innovation Project of JLU (JLUXKJC2021QZ14).

Conflict of Interest

The authors declare no conflict of interest.

Data Availability Statement

Research data are not shared.

Keywords

black phosphorus quantum dots, double hole transport layers, near-infrared light, organic heterojunctions, perovskite solar cells

Received: April 6, 2022

Revised: May 25, 2022

Published online:

- [1] H. Min, D. Lee, J. Kim, G. Kim, K. S. Lee, J. Kim, M. J. Paik, Y. K. Kim, K. S. Kim, M. G. Kim, T. J. Shin, S. I. Seok, *Nature* **2021**, *598*, 444.
- [2] J. Peng, D. Walter, Y. H. Ren, M. Tebyetekerwa, Y. L. Wu, T. Duong, Q. L. Lin, J. T. Li, T. Lu, M. A. Mahmud, O. L. C. Lem, S. Y. Zhao, W. Z. Liu, Y. Liu, H. P. Shen, L. Li, F. Kremer, H. T. Nguyen, D. Y. Choi, K. J. Weber, K. R. Catchpole, T. P. White, *Science* **2021**, *371*, 390.
- [3] S. X. Li, C. Z. Li, M. M. Shi, H. Z. Chen, *ACS Energy Lett.* **2020**, *5*, 1554.
- [4] S. Jeong, S. Seo, H. Yang, H. Park, S. Shin, H. Ahn, D. Lee, J. H. Park, N. G. Park, H. Shin, *Adv. Energy Mater.* **2021**, *11*, 2102236.
- [5] R. Prasanna, T. Leijtens, S. P. Dunfield, J. A. Raiford, E. J. Wolf, S. A. Swifter, J. Werner, G. E. Eperon, C. de Paula, A. F. Palmstrom, C. C. Boyd, M. van Hest, S. F. Bent, G. Teeter, J. J. Berry, M. D. McGehee, *Nat. Energy* **2019**, *4*, 939.
- [6] Q. Y. Chen, J. C. Luo, R. He, H. G. Lai, S. Q. Ren, Y. T. Jiang, Z. X. Wan, W. W. Wang, X. Hao, Y. Wang, J. Q. Zhang, I. Constantinou, C. L. Wang, L. L. Wu, F. Fu, D. W. Zhao, *Adv. Energy Mater.* **2021**, *11*, 10.
- [7] Y. H. Lin, W. Huang, P. Pattanasattayavong, J. Lim, R. Li, N. Sakai, J. Panidi, M. J. Hong, C. Ma, N. Wei, N. Wehbe, Z. Fei, M. Heeney, J. G. Labram, T. D. Anthopoulos, H. J. Snaith, *Nat. Commun.* **2019**, *10*, 4475.
- [8] X. Zhao, C. Yao, T. Liu, J. C. Hamill Jr., G. O. Ngongang Ndjawa, G. Cheng, N. Yao, H. Meng, Y. L. Loo, *Adv. Mater.* **2019**, *31*, 1904494.
- [9] W. Chen, D. Li, S. Chen, S. Liu, Y. Shen, G. Zeng, X. Zhu, E. Zhou, L. Jiang, Y. Li, Y. Li, *Adv. Energy Mater.* **2020**, *10*, 2000851.
- [10] C. Li, H. Wang, F. Wang, T. Li, M. Xu, H. Wang, Z. Wang, X. Zhan, W. Hu, L. Shen, *Light: Sci. Appl.* **2020**, *9*, 31.
- [11] M. Daboczi, J. Kim, J. Lee, H. Kang, I. Hamilton, C. T. Lin, S. D. Dimitrov, M. A. McLachlan, K. Lee, J. R. Durrant, J. S. Kim, *Adv. Funct. Mater.* **2020**, *30*, 2001482.
- [12] C. Wang, Y. Bai, Q. Guo, C. Zhao, J. Zhang, S. Hu, T. Hayat, A. Alsaedi, Z. Tan, *Nanoscale* **2019**, *11*, 4035.
- [13] S. Mahesh, J. M. Ball, R. D. J. Oliver, D. P. McMeekin, P. K. Nayak, M. B. Johnston, H. J. Snaith, *Energy Environ. Sci.* **2020**, *13*, 258.
- [14] M. Jeong, I. W. Choi, E. M. Go, Y. Cho, M. Kim, B. Lee, S. Jeong, Y. Jo, H. W. Choi, J. Lee, J. H. Bae, S. K. Kwak, D. S. Kim, C. Yang, *Science* **2020**, *369*, 1615.
- [15] D. Y. Luo, R. Su, W. Zhang, Q. H. Gong, R. Zhu, *Nat. Rev. Mater.* **2020**, *5*, 44.
- [16] M. M. Tavakoli, J. Zhao, R. Po, G. Bianchi, A. Cominetti, C. Carbonera, J. Kong, *Adv. Funct. Mater.* **2019**, *29*, 1905887.
- [17] A. Al-Ashouri, E. Kohnen, B. Li, A. Magomedov, H. Hempel, P. Caprioglio, J. A. Marquez, A. B. M. Vilches, E. Kasparavicius, J. A. Smith, N. Phung, D. Menzel, M. Grischek, L. Kegelmann, D. Skroblin, C. Gollwitzer, T. Malinauskas, M. Jost, G. Matic, B. Rech, R. Schlatmann, M. Topic, L. Korte, A. Abate, B. Stannowski, D. Neher, M. Stolterfoht, T. Unold, V. Getautis, S. Albrecht, *Science* **2020**, *370*, 1300.
- [18] L. K. Ono, S. Z. Liu, Y. B. Qi, *Angew. Chem., Int. Edit.* **2020**, *59*, 6676.
- [19] Q. Jiang, Z. Ni, G. Xu, Y. Lin, P. N. Rudd, R. Xue, Y. Li, Y. Li, Y. Gao, J. Huang, *Adv. Mater.* **2020**, *32*, 2001581.
- [20] M. Karlsson, Z. Yi, S. Reichert, X. Luo, W. Lin, Z. Zhang, C. Bao, R. Zhang, S. Bai, G. Zheng, P. Teng, L. Duan, Y. Lu, K. Zheng, T. Pullerits, C. Deibel, W. Xu, R. Friend, F. Gao, *Nat. Commun.* **2021**, *12*, 361.
- [21] Q. S. Dong, C. Zhu, M. Chen, C. Jiang, J. Y. Guo, Y. L. Feng, Z. H. Dai, S. K. Yadavalli, M. Y. Hu, X. Cao, Y. Q. Li, Y. Z. Huang, Z. Liu, Y. T. Shi, L. D. Wang, N. P. Padture, Y. Y. Zhou, *Nat. Commun.* **2021**, *12*, 9.
- [22] X. Feng, X. Huang, L. Chen, W. C. Tan, L. Wang, K.-W. Ang, *Adv. Funct. Mater.* **2018**, *28*, 1801524.
- [23] M. Batmunkh, M. Bat-Erdene, J. G. Shapter, *Adv. Energy Mater.* **2017**, *8*, 1701832.
- [24] R. A. Doganov, E. C. O'Farrell, S. P. Koenig, Y. Yeo, A. Ziletti, A. Carvalho, D. K. Campbell, D. F. Coker, K. Watanabe, T. Taniguchi, A. H. Castro Neto, B. Ozilmez, *Nat. Commun.* **2015**, *6*, 6647.
- [25] Z. Sofer, D. Sedmidubsky, S. Huber, J. Luxa, D. Bousa, C. Boothroyd, M. Purnera, *Angew. Chem., Int. Ed. Engl.* **2016**, *55*, 3382.
- [26] M. Batmunkh, K. Vimalanathan, C. Wu, A. S. R. Bati, L. Yu, S. A. Tawfik, M. J. Ford, T. J. Macdonald, C. L. Raston, S. Priya, C. T. Gibson, J. G. Shapter, *Small Methods* **2019**, *3*, 1800521.
- [27] C. Gao, H. Yu, Y. Wang, D. Liu, T. Wen, L. Zhang, S. Ge, J. Yu, *Anal. Chem.* **2020**, *92*, 6822.
- [28] Y. Yang, J. Gao, Z. Zhang, S. Xiao, H. H. Xie, Z. B. Sun, J. H. Wang, C. H. Zhou, Y. W. Wang, X. Y. Guo, P. K. Chu, X. F. Yu, *Adv. Mater.* **2016**, *28*, 8937.
- [29] X. Gong, L. Guan, Q. W. Li, Y. Li, T. Zhang, H. Pan, Q. Sun, Y. Shen, C. Gratzel, S. M. Zakeeruddin, M. Gratzel, M. K. Wang, *Sci. Adv.* **2020**, *6*, 10.
- [30] B. K. Gu, Y. Du, B. Chen, R. Zhao, H. Lu, Q. Y. Xu, C. X. Guo, *ACS Appl. Mater. Interfaces* **2022**, *14*, 11264.

- [31] S. N. Liu, J. K. Lyu, D. L. Zhou, X. M. Zhuang, Z. C. Shi, R. Sun, L. Liu, Y. J. Wu, B. Liu, D. L. Liu, H. W. Song, *Adv. Funct. Mater.* **2021**, *12*, 64711.
- [32] X. F. Lin, P. P. Cheng, Y. W. Zhang, W. Y. Tan, D. S. Yu, G. B. Yi, Y. G. Min, *Sol. Energy* **2020**, *206*, 793.
- [33] X. F. Lin, Y. Y. Wang, J. Y. Wu, Z. L. Tang, W. J. Lin, L. Nian, G. B. Yi, *ACS Appl. Energy Mater.* **2021**, *4*, 5905.
- [34] J. Pang, A. Bachmatiuk, Y. Yin, B. Trzebicka, L. Zhao, L. Fu, R. G. Mendes, T. Gemming, Z. Liu, M. H. Rummeli, *Adv. Energy Mater.* **2018**, *8*, 1702093.
- [35] T. Leijtens, K. A. Bush, R. Prasanna, M. D. McGehee, *Nat. Energy* **2018**, *3*, 828.
- [36] J. Werner, L. Barraud, A. Walter, M. Bräuninger, F. Sahli, D. Sacchetto, N. Tétreault, B. Paviet-Salomon, S.-J. Moon, C. Allebé, M. Despeisse, S. Nicolay, S. De Wolf, B. Niesen, C. Ballif, *ACS Energy Lett.* **2016**, *1*, 474.
- [37] H. Shen, T. Duong, J. Peng, D. Jacobs, N. Wu, J. Gong, Y. Wu, S. K. Karuturi, X. Fu, K. Weber, X. Xiao, T. P. White, K. Catchpole, *Energy Environ. Sci.* **2018**, *11*, 394.
- [38] J. A. Christians, R. C. Fung, P. V. Kamat, *J. Am. Chem. Soc.* **2014**, *136*, 758.
- [39] R. A. Jagt, T. N. Huq, S. A. Hill, M. Thway, T. Liu, M. Napari, B. Roose, K. Gałkowski, W. Li, S. F. Lin, S. D. Stranks, J. L. MacManus-Driscoll, R. L. Z. Hoye, *ACS Energy Lett.* **2020**, *5*, 2456.
- [40] Z. Sun, H. Xie, S. Tang, X. F. Yu, Z. Guo, J. Shao, H. Zhang, H. Huang, H. Wang, P. K. Chu, *Angew. Chem., Int. Ed. Engl.* **2015**, *54*, 11526.
- [41] N. Fu, C. Huang, P. Lin, M. Zhu, T. Li, M. Ye, S. Lin, G. Zhang, J. Du, C. Liu, B. Xu, D. Wang, S. Ke, *J. Mater. Chem. A* **2018**, *6*, 8886.
- [42] J. Zhang, B. Xu, L. Yang, C. Ruan, L. Wang, P. Liu, W. Zhang, N. Vlachopoulos, L. Kloof, G. Boschloo, L. Sun, A. Hagfeldt, E. M. J. Johansson, *Adv. Energy Mater.* **2018**, *8*, 1701209.
- [43] W. Budiawan, K. W. Lai, P. Karuppuswamy, T. S. Jadhav, Y. A. Lu, K. C. Ho, P. C. Wang, C. C. Chang, C. W. Chu, *ACS Appl. Mater. Interfaces* **2020**, *10*, 021.
- [44] K. Jiang, J. Wang, F. Wu, Q. Xue, Q. Yao, J. Zhang, Y. Chen, G. Zhang, Z. Zhu, H. Yan, L. Zhu, H. L. Yip, *Adv. Mater.* **2020**, *32*, 1908011.
- [45] C. Zuo, L. Ding, *Angew. Chem., Int. Ed. Engl.* **2021**, *60*, 11242.
- [46] L. Wen, Y. Rao, M. Zhu, R. Li, J. Zhan, L. Zhang, L. Wang, M. Li, S. Pang, Z. Zhou, *Angew. Chem., Int. Ed. Engl.* **2021**, *60*, 17356.
- [47] S. Wu, Z. Li, J. Zhang, X. Wu, X. Deng, Y. Liu, J. Zhou, C. Zhi, X. Yu, W. C. H. Choy, Z. Zhu, A. K. Jen, *Adv. Mater.* **2021**, *33*, 2105539.
- [48] Q. Hu, W. Chen, W. Yang, Y. Li, Y. Zhou, B. W. Larson, J. C. Johnson, Y.-H. Lu, W. Zhong, J. Xu, L. Klivansky, C. Wang, M. Salmeron, A. B. Djurišić, F. Liu, Z. He, R. Zhu, T. P. Russell, *Joule* **2020**, *4*, 1575.
- [49] W. Chen, H. Sun, Q. Hu, A. B. Djurišić, T. P. Russell, X. Guo, Z. He, *ACS Energy Lett.* **2019**, *4*, 2535.
- [50] S. Dong, Y. Liu, Z. Hong, E. Yao, P. Sun, L. Meng, Y. Lin, J. Huang, G. Li, Y. Yang, *Nano Lett.* **2017**, *17*, 5140.
- [51] Y. Wu, Y. Gao, X. Zhuang, Z. Shi, W. Bi, S. Liu, Z. Song, C. Chen, X. Bai, L. Xu, Q. Dai, H. Song, *Nano Energy* **2020**, *77*, 105181.
- [52] K. Nishimura, M. A. Kamarudin, D. Hirotani, K. Hamada, Q. Shen, S. Iikubo, T. Minemoto, K. Yoshino, S. Hayase, *Nano Energy* **2020**, *74*, 104858.
- [53] L. Xie, Z. Cao, J. Wang, A. Wang, S. Wang, Y. Cui, Y. Xiang, X. Niu, F. Hao, L. Ding, *Nano Energy* **2020**, *74*, 104846.
- [54] H. Guo, H. Zhang, C. Shen, D. Zhang, S. Liu, Y. Wu, W. H. Zhu, *Angew. Chem., Int. Ed. Engl.* **2021**, *60*, 2674.
- [55] H. Zhu, Z. Shen, L. Pan, J. Han, F. T. Eickemeyer, Y. Ren, X. Li, S. Wang, H. Liu, X. Dong, S. M. Zakeeruddin, A. Hagfeldt, Y. Liu, M. Grätzel, *ACS Energy Lett.* **2020**, *6*, 208.
- [56] M. Jošt, B. Lipovšek, B. Glažar, A. Al-Ashouri, K. Brecl, G. Matič, A. Magomedov, V. Getautis, M. Topič, S. Albrecht, *Adv. Energy Mater.* **2020**, *10*, 2000454.
- [57] A. Mei, Y. Sheng, Y. Ming, Y. Hu, Y. Rong, W. Zhang, S. Luo, G. Na, C. Tian, X. Hou, Y. Xiong, Z. Zhang, S. Liu, S. Uchida, T.-W. Kim, Y. Yuan, L. Zhang, Y. Zhou, H. Han, *Joule* **2020**, *4*, 2646.
- [58] W. Mao, C. R. Hall, S. Bernardi, Y. B. Cheng, A. Widmer-Cooper, T. A. Smith, U. Bach, *Nat. Mater.* **2021**, *20*, 55.
- [59] L. Shen, S. Shi, S. Roy, X. Yin, W. Liu, Y. Zhao, *Adv. Funct. Mater.* **2020**, *31*, 2006066.
- [60] A. D. Taylor, Q. Sun, K. P. Goetz, Q. Z. An, T. Schramm, Y. Hofstetter, M. Litterst, F. Paulus, Y. Vaynzof, *Nat. Commun.* **2021**, *12*, 11.
- [61] D. J. Xue, Y. Hou, S. C. Liu, M. Y. Wei, B. Chen, Z. R. Huang, Z. B. Li, B. Sun, A. H. Proppe, Y. T. Dong, M. I. Saidaminov, S. O. Kelley, J. S. Hu, E. H. Sargent, *Nat. Commun.* **2020**, *11*, 8.
- [62] Y. Ying, G. A. O. Jing, C. U. I. Jia-Rui, G. U. O. Xue-Yi, **2015**, 30.
- [63] T. T. Zhou, T. Zhang, *Small Methods* **2021**, *5*, 32.
- [64] Q. Wang, B. Chen, Y. Liu, Y. H. Deng, Y. Bai, Q. F. Dong, J. S. Huang, *Energy Environ. Sci.* **2017**, *10*, 516.
- [65] X. P. Zheng, B. Chen, J. Dai, Y. J. Fang, Y. Bai, Y. Z. Lin, H. T. Wei, X. C. Zeng, J. S. Huang, *Nat. Energy* **2017**, *2*, 9.